JOURNAL OF PROPULSION AND POWER
Vol. 10, No. 1, Jan.–Feb. 1994

Computational Investigation of Circular-to-Rectangular Transition Ducts

S. Paul Pao* and John R. Carlson‡
NASA Langley Research Center, Hampton, Virginia 23665
and
Khaled S. Abdol-Hamid†
Analytical Services and Materials, Inc., Hampton, Virginia 23605

The objective of this article is to demonstrate the feasibility of conducting three-dimensional Navier-Stokes calculations for a family of three short circular-to-rectangular transition ducts, and to establish quantitative measures of accuracy for duct design applications. A three-dimensional multiblock Navier-Stokes code, PAB3D, was used in this study. The transition ducts were designed to connect a typical circular engine exhaust to a high aspect ratio rectangular supersonic nozzle. The transitional cross sections were represented by superellipses. The rectangular supersonic nozzle was included in the flow path for the numerical analysis such that the computed results can be directly compared to existing experimental results for these ducts. Internal flow solutions were computed by using both laminar viscosity and a low Reynolds number two-equation k-ε turbulence modeling. Static pressure coefficient distributions, discharge coefficient, and thrust ratio quantities were calculated according to the on-design operating conditions for the nozzle. Good agreement between predicted surface static pressures and experimental data was observed. Nozzle performance was predicted to within experimental accuracy for both the laminar and the k-ε solutions.

Nomenclature

A = constant duct cross sectional area, cm^2
a = semimajor axis of superellipse, cm
b = semiminor axis of superellipse, cm
d = diameter of transition duct entrance, cm
e = total energy per unit volume, J/m^3
F = gross thrust along body axis, N
F_i = ideal isentropic gross thrust, N
l = length from duct-connect station to duct-exit station, cm
l_n = nozzle reference length, cm
p = local static pressure, Pa
$p/p_{t,j}$ = normalized static pressure
$p_{t,j}$ = jet total pressure, Pa
R = gas constant (γ = 1.40), 287.3 J/kg K
$T_{t,j}$ = jet total temperature, K
u = velocity in streamwise direction, m/s
v = velocity in lateral direction, m/s
w = velocity in vertical direction, m/s
w_i = ideal mass flow rate, kg/s
w_p = calculated or measured mass flow rate, kg/s
x = axial distance, positive downstream, cm
y = lateral distance from model centerline, cm
y^+ = dimensionless wall distance
z = vertical distance from model centerline, cm
γ = ratio of specific heats, 1.40 for air
η = exponent of superellipse
ρ = density, kg/m^3

Presented as Paper 91-3342 at the AIAA 9th Applied Aerodynamics Conference, Baltimore, MD, Sept. 23–25, 1991; received Aug. 31, 1992; revision received March 2, 1993; accepted for publication May 17, 1993.

*Aerospace Engineer, Propulsion Aerodynamics Branch, Applied Aerodynamics Division. Associate Fellow AIAA.
†Senior Scientist. Member AIAA.
‡Aerospace Engineer, Propulsion Aerodynamics Branch, Applied Aerodynamics Division. Senior Member AIAA.

Introduction

SINCE the early introduction of the rectangular nozzle concept,[1] much progress has been made in the effective utilization and integration of rectangular nozzles with the airframe for aircraft propulsion. Although external drag levels of integrated rectangular nozzles can be maintained at a level similar to those of axisymmetric configurations, poor internal flow design could produce offsetting performance losses. Ideally, the transition from the axisymmetric engine flow to the rectangular exhaust system should be short to minimize the duct weight, but long enough to prevent flow separation that may adversely affect surface heat transfer and nozzle performance.

The effect of duct length on the internal performance of a high-aspect ratio nozzle was investigated by Burley et al.,[2] by measuring the surface pressure and the overall performance of several circle-to-rectangle transition ducts. The measurements were conducted in the static test facility of the 16-ft transonic tunnel at NASA Langley. An analysis of the internal wall static pressure using a potential flow panel method[3] was included in Ref. 2. Flow calculations in ducts with superelliptic cross sections were often reported in the literature.[4–8] However, few previous investigations had used ducts as short or as high an aspect ratio as those tested by Burley et al.[2] The objective of the present study is to demonstrate the feasibility of conducting a detailed numerical analysis for attached and separated flows in such ducts, and to establish quantitative measures of accuracy for the computational method.

A three-dimensional multiblock/multizone Navier-Stokes code, PAB3D, is used in this study.[9,10] Predictions of nozzle internal flows using this code were found to be highly accurate.[11,12] Recent enhancements to the PAB3D code include an addition of a two-equation k-ε turbulence model by Abdol-Hamid et al.,[13] and a module for performance calculation was added by Carlson.[14] The low-Reynolds number option of the k-ε turbulence model was used for the present study. The

performance module has proven to be highly accurate in predicting nozzle discharge coefficients, thrust, and vectoring forces for both axisymmetric- and nonaxisymmetric-type nozzle geometries. Both of these added capabilities are important to the present study.

Part of the difficulties for analyzing these ducts with special geometry is grid generation. A compact grid generation code was developed for this study at NASA Langley to satisfy the unusual geometrical requirements. A two-block grid with mixed polar and Cartesian types was designed such that the grid cell aspect ratio and orthogonality were maintained within a reasonable range for all the duct cross sections. The first block with a polar layout covered a ring-shaped region near the duct wall. It was surface fitted to the internal duct wall surface. The second block was Cartesian which covered the central portion of the duct. A one-to-one grid matching was enforced at the interfaces between these two blocks. The volume grid was generated by means of transfinite interpolation. The volume grid covered one quadrant of the duct configuration by assuming flow symmetry at the vertical and horizontal quadrant boundaries.

Flow calculations were performed at the nozzle design condition for three ducts chosen from Ref. 2. These were constant area ducts with similar cross sections, but different length to diameter ratios. The computed flow solutions were compared with experimental measurements of the normalized wall static pressure distributions $p/p_{t,j}$, nozzle discharge coefficient w_p/w_i, and internal thrust ratio F/F_i. Flow uniformity and the extent of flow separation in the duct according to the flow solutions were also examined. As experimental data were limited for these parameters, it is hoped that the computational analysis will shed some light on flow properties which are important for the design of exhaust transition ducts.

Transition Duct Model Configurations

A single-engine nozzle model was tested by Burley et al.[2] in the static facility of the 16-ft transonic tunnel at the NASA Langley research center to investigate the effect of internal transition duct length on nozzle performance. A sketch of the duct model is presented in Fig. 1. The transition duct was designed by using a sequence of constant-area, superelliptic cross sections.

$$(y/a)^\eta + (z/b)^\eta = 1$$

Circles, with $a = b$ and $\eta = 2$, and rectangles, with $\eta \to \infty$, are included in this family of curves. For practical purposes, the shape of the curve was considered a rectangle for $\eta \geq 50$.

The model scaled exhaust transition duct entrance was circular with a diameter of 12.863 cm, and the exit was a rectangle which had dimensions of 28.682 × 4.531 cm, with an aspect ratio of 6.331. The maximum height and width of the duct cross section were represented by cubic functions which

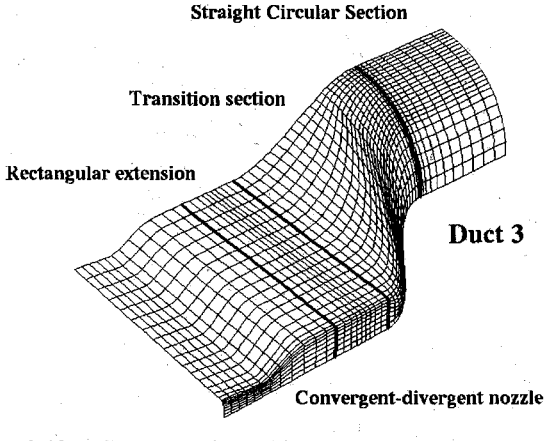

Fig. 1 Grid configuration of transition duct and nozzle combination.

Table 1 Transition duct geometry

Constant area	129.941 cm²
Entrance circle	
Diameter	12.863 cm
Exit rectangle	
Width	28.682 cm
Height	4.531 cm
Aspect ratio	6.331
Duct lengths	
Duct 2	12.863 cm
Duct 3	9.647 cm
Duct 4	6.431 cm
Nozzle	
Length	7.394 cm
Throat height	0.958 cm
Exit height	1.227 cm
Throat aspect ratio	14.976

were chosen to achieve zero slopes at their end points. These functions defined a and b of the superellipse. The exponent of the superellipse was calculated from an implicit function relating the quantities a, b, and η to A of the superellipse

$$A = \frac{\Gamma(1/\eta)^2}{\Gamma(2/\eta)}\,(2/\eta)\cdot(4ab)$$

where $\Gamma(\ )$ denotes the gamma function. The transition ducts in this family had the same cross-sectional shape at a given value of x/l. Their overall lengths in the flow direction were different: l/d was 1.0, 0.75, and 0.5 for duct 2, duct 3, and duct 4, respectively. The serial designation for these ducts were the same as Ref. 2 in which two other ducts with different design characteristics, 1 and 5, were also included. The exhaust nozzle used with all three ducts was a convergent-divergent, two-dimensional type with a circular-arc throat contour, straight divergent flaps and flat sidewalls. The nozzle was designed for an area expansion ratio of 1.281. The controlling dimensions of the transition ducts and nozzle are summarized in Table 1.

Details of the nozzle geometry and pressure orifice locations can be found in Ref. 2. In the experimental setup, the total flow path length for all the three ducts, i.e., from the upstream duct connect to the nozzle exit face, was identical. The longest duct, duct 2, fitted between the duct connect at the end of the instrumentation section and the nozzle connect station. For the shorter ducts 3 and 4, a constant cross-sectional rectangular extension fitted between the end of the transition section and the nozzle connect station made up the difference in length.

Computational Procedure

Solver and Boundary Conditions

The three-dimensional Navier-Stokes code, PAB3D, was used for flow analysis. In the flow path through the transition duct and the nozzle, both subsonic and supersonic regions, with the possibility of flow separation, were expected. The Roe scheme in the PAB3D code was used for obtaining numerical solutions. Since the inflow was subsonic, $p_{t,j}$ and $T_{t,j}$ were specified as boundary conditions at the inflow face. An extrapolation outflow boundary condition was used at the supersonic nozzle exit. A no-slip boundary condition was used on the internal walls of the duct and the nozzle. Only one quadrant of the duct was represented in the grid domain. Therefore, mirror image symmetry conditions for the flowfield were imposed at the quadrant boundaries.

Two different methods were used to represent the viscous effects in the flowfield: laminar viscosity and the low Reynolds number k-ε turbulence model by Jones and Launder.[15] Although several algebraic turbulence models were also avail-

able in the PAB3D code, those were not used in this study for two reasons. The boundary layer, when separated, may fill the entire height at the extreme ends of the high aspect ratio cross sections of the duct. The length scale of the algebraic turbulence model would therefore become ambiguous. A second factor had to do with the two-block mesh structure. In regions of extensive flow separation, the separated flow region may cross a block boundary. There was no convenient way to continue the turbulence parameters from one grid block to another.

Grid Generation

An algebraic grid generation code was developed to deal with the special geometrical requirements for a continuous transition from a circular engine to a high aspect ratio rectangular nozzle connection. The overall mesh configuration is shown in Fig. 1. There are four distinct segments along the axial direction: 1) a constant diameter circular entrance section, 2) the transition section, 3) followed by a rectangular extension, and 4) finally the two-dimensional convergent-divergent nozzle. Horizontal and vertical plane flow symmetry was assumed to reduce the total number of grid points.

Because of the drastic changes in cross-sectional shape within a short distance in the flow direction, a single-block mesh topology is incapable of providing a smooth description of both the central region of the duct and the boundary layer at the wall. A two-block grid which combined a 36 × 15 Cartesian mesh in the center of the duct and a 50 × 31 polar mesh fitted to the duct wall was used to provide smooth discretization of the entire volume inside the transition duct. The polar mesh contained 31 grids in directions normal to the wall. The first 21 grids covered approximately the estimated momentum thickness of an attached boundary layer. Sample cross sections of this grid are shown in Fig. 2. The polar-type mesh, fitted to the duct and nozzle internal surface, provided a continuous boundary-layer grid for the entire configuration. The polar grid was matched one-to-one with the H-grid at the grid interface. Since the polar mesh block was relatively thin as compared to the circumference and the length of the duct surface, local mesh orthogonality was easily maintained. Similarly, the central H-type mesh responded to the rapidly increasing aspect ratio of the duct cross section by merely adjusting the aspect ratio of individual cells without sacrificing orthogonality. The grid spacing around the circumference was determined within the grid code based on the arc length and curvature for each cross section. The volume grid was generated algebraically using a transfinite interpolation algorithm.

Streamwise grid densities were 12, 42, and 26 grid planes in the constant diameter section, the transition duct, and the nozzle, respectively. The number of grid planes in the rectangular extension between the transition duct and the nozzle varied according to its length requirement: none for duct 2, 16 for duct 3, and 36 for duct 4. The largest grid, duct 4, had a total of 240,000 grid points. For the given duct geometry and expected flow velocities, the Reynolds number based on duct length was approximately 0.64×10^6 in the transition section based on duct length, and approximately 3.5×10^6 near the nozzle throat. The normal distance of the first grid point from the wall corresponded to a value of y^+ less than 2. However, the overall density of the boundary-layer grid was marginal. The first three grid intervals near the wall were made equal, while the next 18 grid intervals were stretched exponentially away from the wall to fill a height equal to a nominal value for the momentum thickness.

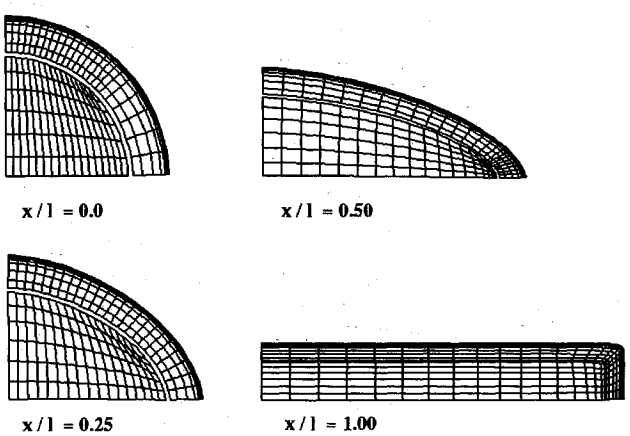

Fig. 2 Transition duct grid cross sections.

A starting solution for each configuration was estimated by solving the one-dimensional isentropic flow equations. The Mach number distribution along the axis of the duct was computed according to the cross-sectional area distribution. A sonic condition was assumed at the nozzle throat. On-design jet total pressure and temperature values were chosen to construct the conservative quantities ρ, ρu, ρv, ρw, and ρe as described in Ref. 11. Furthermore, an approximate boundary-layer velocity distribution was specified for the starting solution.

Calculation of Performance

Since the main purpose of the transition duct is to provide an efficient flow path from the circular engine exhaust duct to the high aspect ratio rectangular nozzle, the prediction of mass flow and thrust performances are very important. In the performance module, the cell centered quantities of the solution are extrapolated to the outflow face of the nozzle and integrated to calculate F, which is the sum of a momentum thrust and the net pressure force at that location. Nozzle w_p was determined by the statistical average of the mass flow through several grid plane cross sections across the flow. The standard deviation of mass flow from the average was taken as one of the indicators of the numerical convergence of the solution. w_i was determined from the isentropic flow equations and is used to normalize the predicted mass flow of the solution. F_i is determined from the isentropic flow equations according to the nozzle pressure ratio, jet total pressure, total temperature, and the computed mass flow rate.

The flow conditions for the computational analysis were chosen to correspond to the experiments reported in Ref. 2 where the transition duct and nozzle combinations were tested by utilizing high-pressure air exhausting into static air. For the experimental data, the nozzle discharge coefficient was determined from experimentally measured $T_{t,j}$, $p_{t,j}$ and mass flow rate. The thrust ratio F/F_i was determined from experimentally measured axial force F, divided by F_i, which was computed according to the measured mass flow.

Results and Discussion

Two sets of solutions to the three-dimensional Navier-Stokes equations were obtained for all three transition ducts using either the laminar viscosity or the low Reynolds number two-equation k-ε turbulence model. The residue in the solver algorithm, mass flow, and thrust force produced by the nozzle were used for monitoring the convergence of the numerical solutions. The execution time for the solutions using the k-ε turbulence model is approximately 38 μs per grid point per iteration on a Cray YMP computer. The solution reached an accepted level of convergence at 2500 iterations for most cases. However, some cases were calculated to twice the number of iterations. A solution was considered converged when the variations in mass flow through the duct and the thrust force produced by the nozzle had fallen below 0.1%. A typical case took 4.5–6 h of Cray YMP to converge.

Figure 3 shows the static pressure distribution on the wall of duct 2 to illustrate basic flow properties of the transition section. As the transition duct height decreases, the pressure increases initially at the top of the cross sections. However,

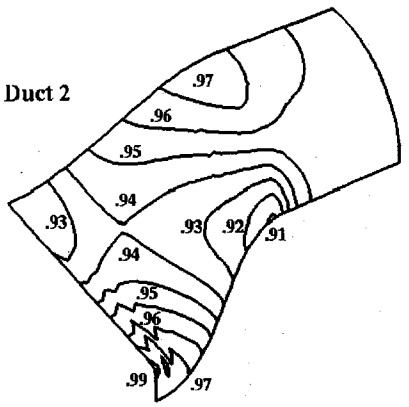

Fig. 3 Overall static pressure distribution on the wall of duct 2, $p/p_{t,j}$.

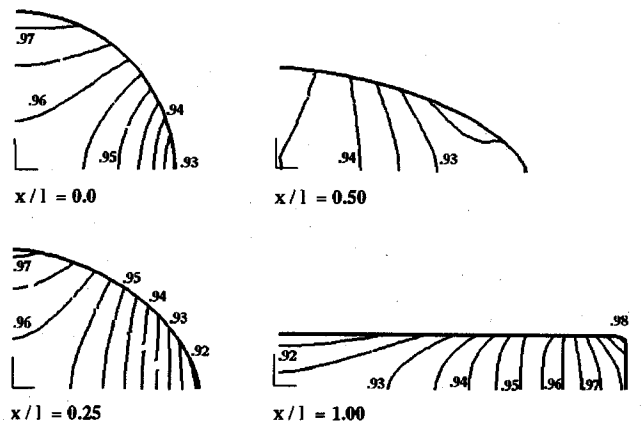

Fig. 4 Static pressure distribution on selected cross sections in duct 2, $p/p_{t,j}$.

as the flow accelerates downstream, the static pressure decreases to a value below its average value in the initial circular section. On the side of the duct, the flow accelerates rapidly as soon as the duct width begins to expand. A strong local low-pressure region can be seen in Fig. 3. The static pressure does not recover to a value above the initial average until a location beyond $x/l = 0.75$. Typical cross-sectional pressure distributions for the same duct are shown in Fig. 4. At $x/l = 0.0$ and 0.25, the pressure distributions exhibit a polar asymmetric pattern: a pressure increase at the top is matched by a corresponding decrease at the side of the section. For $x/l \geq 0.50$, however, a dominant horizontal pressure gradient is established. There are two noteworthy features at the exit section of the transition duct where $x/l = 1.0$. The lowest pressure occurs in a thin horizontal layer near the top center of the rectangular cross section. This flow feature persists for the remainder of the flow path. The second feature is the high-pressure recovery at the extreme end of the high aspect ratio cross sections. As one may expect, the increased pressure near the side wall is a warning of imminent flow separation.

The laminar flow solution and the k-ε turbulence model solution can be quite different in detail. Essentially, flow separations near the duct sidewall were much more extensive in the laminar solutions than those contained in the k-ε solutions. For the laminar solution, a small sidewall separation started in duct 2, and extensive regions of flow separations near the sidewall were observed in the solutions of ducts 3 and 4. Once extensive flow separation occurred, the velocity distribution inside the duct appeared to be oscillatory in the streamwise and spanwise directions. On the other hand, the k-ε flow solution for duct 2 was attached througout the duct. A thin separated flow region along the sidewall appeared in duct 3, while extensive flow separation similar to the laminar solution was observed in duct 4. It is difficult to judge from the computed flow character that one solution is better than the other. It was noted by examination of the early solution development that the laminar flow started to separate as soon as it entered the transition section. The predicted early separation was not in agreement with experimental pressure data of Ref. 2. The initial location of flow separation and the pressure distributions in the k-ε solution appeared to agree better with the experimental data. Some computed results of the k-ε solutions for ducts 2, 3, and 4 are shown in Fig. 5. The u-velocity component distribution illustrates the details of flow separation near the sidewall. The static pressure distributions in Fig. 5 show good pressure recoveries in duct 2 and duct 3, but not in duct 4.

A comparison between the measured and the computed normalized wall static pressure distribution in duct 4 is shown in Fig. 6. Quantitatively, the pressure distribution agreement is within 3% along the sidewall of the duct. Paradoxically, the differences in the normalized static pressure in the central portion of the duct is as high as 6%, although the gradients represented by the contour lines are similar between the k-ε solution and the measured data of Ref. 2.

Figure 7 shows the comparison of sidewall normalized static pressure between the experimental data[2] and the computed solutions. The static pressure orifices in Ref. 2 were located at various x/l along the center of the transition duct sidewall. For duct 2, the computed results are between 1–3% above the measured data. For duct 3, the maximum difference was 4%. Although the k-ε solution is relatively smooth, the laminar solution shows several cycles of pressure fluctuation along

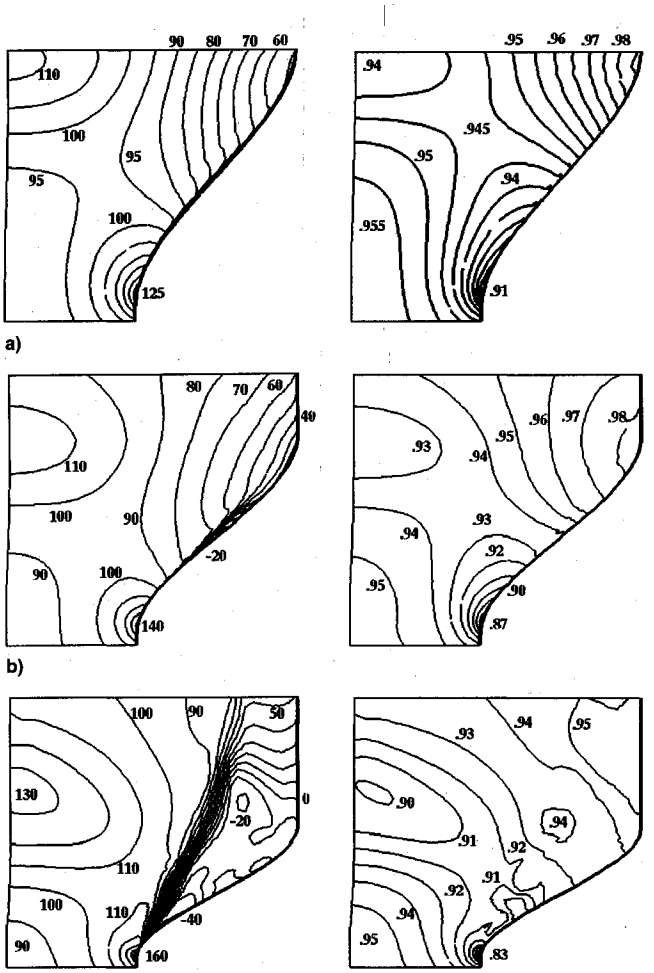

Fig. 5 Axial velocity and static pressure distributions in the horizontal plane of symmetry for the k-ε solutions, m/s: a) duct 2, b) duct 3, and c) duct 4.

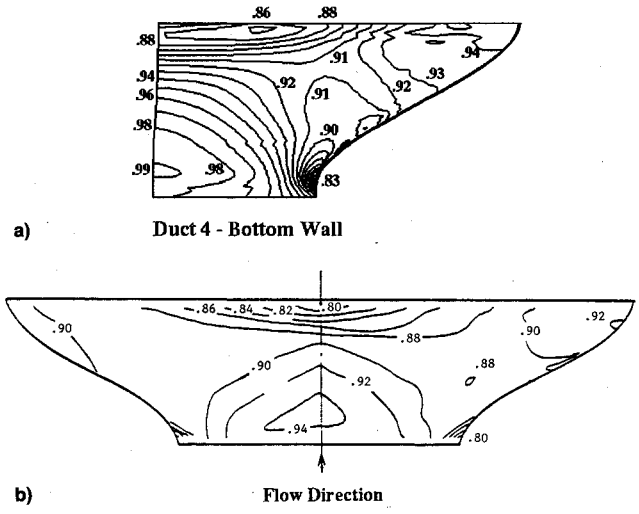

Fig. 6 Computed and measured static pressure distribution on the duct 4 bottom wall, $p/p_{t,j}$: a) computed solution and b) measured data.

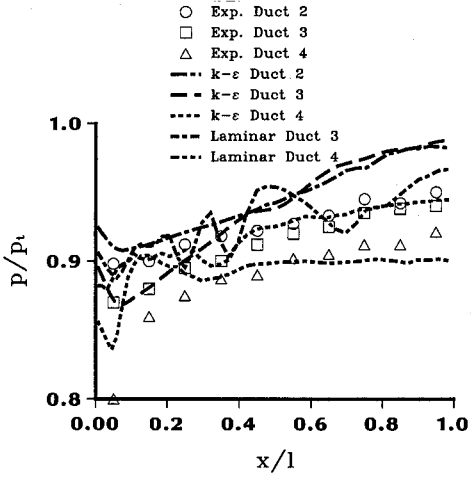

Fig. 7 Computed and measured static pressure on the duct sidewall along the horizontal plane of symmetry.

the x direction. The agreement in pressure level is within 2% for the most part in duct 4. Both the laminar and the k-ε solutions show some degree of pressure fluctuation. In duct 3 and duct 4, the k-ε normalized pressure values came much closer to the measured data near the point of maximum flow acceleration around the expansion corner near the duct entrance. Hence, it is likely that the k-ε turbulence modeling would provide a better solution for the analysis of boundary-layer flow separation in a transition duct. Static pressure comparisons along the center of the bottom wall are shown in Fig. 8. The trends of computed pressure distribution are in good agreement with the experimental data for all three ducts. However, the computed static pressure values are approximately 3% higher than the measured data.

Since the 2-D C-D nozzle was an integral part of each of the model configurations, it is of interest to examine the results for the flowfield in the nozzle. Figure 9 shows the measured normalized static pressure and the computed k-ε solutions along the center of the bottom wall of the 2-D C-D nozzle. Data for all three duct configurations are shown in Fig. 9. Nearly perfect agreement is shown between computation and experimental data for all cases. The computed flow solution across the width of the nozzle is not uniform. The static pressure near the nozzle sidewall is slightly higher than the center. Although there is no data to verify the flow distribution across the nozzle, this nonuniformity is consistent with the normalized static pressure distribution in duct 4 as shown in Fig. 6.

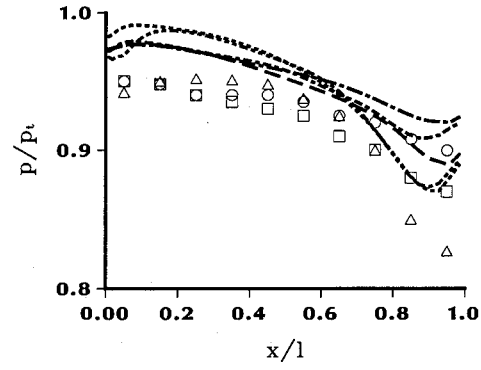

Fig. 8 Computed and measured static pressure along the duct bottom wall centerline.

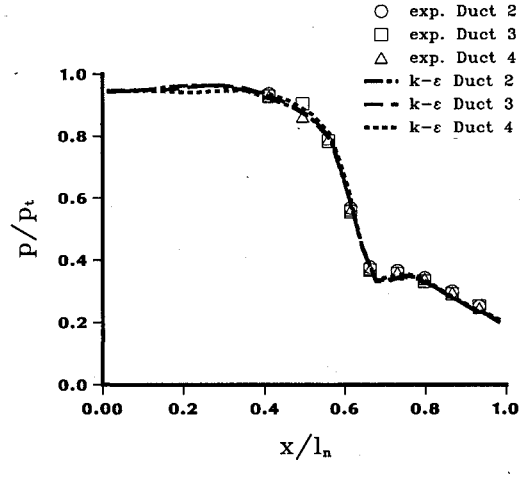

Fig. 9 Computed and measured static pressure along the nozzle bottom wall centerline.

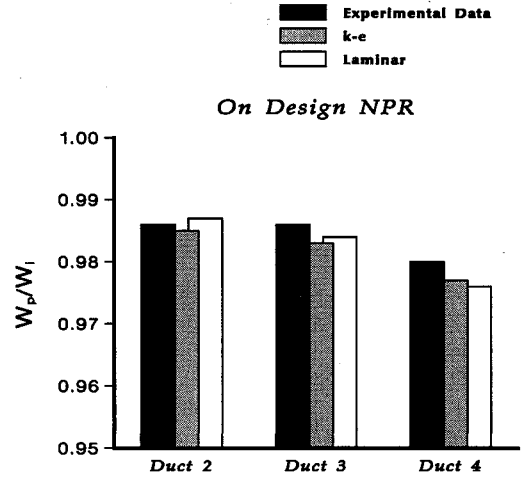

Fig. 10 Computed and measured mass flow discharge coefficient.

The difference in the accuracy of the predicted normalized static pressure in the transition duct vs those predicted in the nozzle section can be attributed to grid resolution. The boundary grid cells were sized according to nominal values of the length and the velocities in the transition duct. In the upstream portion of the flow path, the boundary layer was thinner than anticipated. As a result, the grid resolution was coarse. The higher predicted normalized wall static pressure indicated a higher pressure recovery in the boundary resulting from a lack of viscous dissipation. On the other hand, both the boundary-layer thickness and the Reynolds number values were higher in the 2D-CD section. Sufficient grid resolution in the boundary-layer grid had resulted in much better static

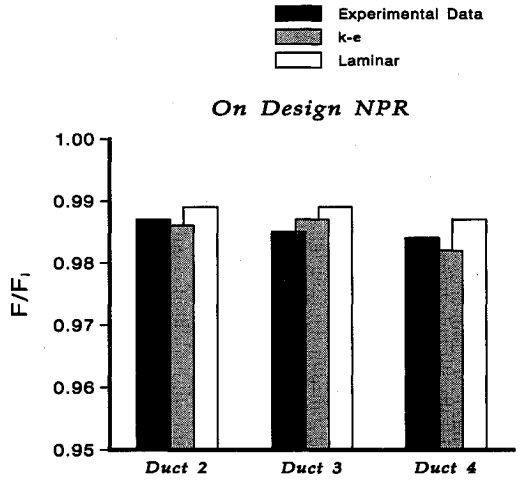

Fig. 11 Computed and measured nozzle thrust ratio.

pressure coefficient prediction. Due to the substantial resources requirements for using the Navier-Stokes code, these cases were not recomputed with a higher resolution grid.

Finally, comparisons of overall mass flow and thrust performance are shown in Figs. 10 and 11. The predicted mass flow discharge coefficient agreed with the measured data within 0.5%, which is less than or equal to the margin of experimental error. No significant differences in predictive accuracy was found between the laminar and the k-ε solutions. The thrust coefficient predicted by the laminar solution was within 1% of the experimental data, while the k-ε solution was within 0.5% of the data.

In all three cases, the predicted thrust coefficient for the laminar solution was higher than the corresponding values predicted by the k-ε solution. This trend is consistent with flow physics where a higher thrust loss is expected in the turbulent boundary layer of the k-ε solution.

Concluding Remarks

This investigation has demonstrated that a Navier-Stokes analysis is feasible for transition duct/exhaust nozzle combination with a properly designed computational mesh. Exact geometries of three transition ducts which were used in an experimental study were used in this numerical study of the transition duct internal flow characteristics. Reasonable agreements were obtained for wall static pressure coefficient comparisons in the transition duct between the computed solutions and the measured data. Static pressure coefficient comparisons in the 2-D C-D nozzle section were excellent. Excellent agreement between computed and measured mass flow and thrust performance were also obtained.

Based on the computed results for ducts with similar cross sections but different overall duct length, the numerical analysis appeared to be sensitive enough to determine the onset of flow separation along the diverging sidewall of the transition duct. Laminar viscous stress modeling for the entire flowfield of the duct would not be typically appropriate for flow with a Reynolds number on the order of one million, particularly with the flow separation that occurs in these ducts. Prediction of viscous turbulent dominated flow phenomena such as the location and extent of separated flow would be incorrectly calculated with laminar stresses. Interestingly though, fairly small differences in predicted mass flow and performance were observed for these nozzles, owing to the fact that thrust producing flow was largely inviscid in character. The geometric contraction upstream of the nozzle throat substantially reduced the boundary-layer thickness of the flow at the throat, thereby reducing the effects of upstream turbulence. In addition, both the laminar and turbulent flow solutions must similarly fill the nozzle, despite the differences in detail of the separated flow regions, resulting in roughly equivalent thrust performance levels.

The k-ε solutions are more consistent in simulating the experimental measurements as the laminar flow model was unable to model the duct internal flow separation properly. The consistency of the solution is affected by several factors: the Reynolds number of the internal flow, the strong adverse pressure gradient near the sidewall, and the boundary-layer grid density. It is concluded that grid densities in the boundary layer higher than those specified for the present study should be used in order to achieve a better accuracy for wall static pressure coefficient predictions and the simulation of the separated flow.

Acknowledgments

The authors would like to acknowledge Kenji Uenishi and William M. Turner of the General Electric Aircraft Engines for making the k-ε turbulence model available for this investigation, and for their helpful suggestions.

References

[1]Capone, F. J., "The Nonaxisymmetric Nozzle—It is for Real," AIAA Paper 79-1810, Aug. 1979.

[2]Burley, J. R., II, Bangert, L. S., and Carlson, J. R., "Static Investigation of Circular-to-Rectangular Transition Ducts for High-Aspect-Ratio Nonaxisymmetric Nozzles," NASA TP-2534, March 1986.

[3]Hawk, J. D., and Bristow, D. R., "Development of MCAERO Wing Design Panel Method with Interactive Graphics Module," NASA CR-3775, April 1984.

[4]Mayer, E., "Effect of Transition in Cross-Sectional Shape on the Development of the Velocity and Pressure Distribution of the Turbulence Flow in Pipes," NACA TM-903, Aug. 1939.

[5]Patrick, W. P., and McCormick, D. C., "Circular to Rectangular Duct Flows: A Benchmark Experimental Study," Society of Automotive Engineers TP 871776, 1987.

[6]Patrick, W. P., and McCormick, D. C., "Laser Velocimeter and Total Pressure Measurements in Circular to Rectangular Transitional Ducts," United Technology Research Center, Rept. 87-41, East Hartford, CT, June 1988.

[7]Reichert, B. A., Hingst, W. R., and Okiishi, T. H., "An Experimental Trace Gas Investigation of Fluid Transport and Mixing in a Circular-to-Rectangular Transition Duct," AIAA Paper 91-2370, June 1991.

[8]Sirbaugh, J. R., and Reichert, B. A., "Computation of a Circular-to-Rectangular Transition Duct Flow Field," AIAA Paper 91-1741, June 1991.

[9]Abdol-Hamid, K. S., and Compton, W. B., III, "Supersonic Navier-Stokes Simulations of Turbulent Afterbody Flows," AIAA Paper 89-2194, June 1989.

[10]Abdol-Hamid, K. S., "The Application of 3D Space Marching Scheme for the Prediction of Supersonic Free Jets," AIAA Paper 89-2897, July 1989.

[11]Abdol-Hamid, K. S., "Application of a Multiblock/Multizone Code (PAB3D) for the Three-Dimensional Navier-Stokes Equations," AIAA Paper 91-2155, June 1991.

[12]Carlson, J. R., and Abdol-Hamid, K. S., "Prediction of Internal Performance for Two-Dimensional Convergent-Divergent Nozzles," AIAA Paper 91-2369, June 1991.

[13]Abdol-Hamid, K. S., Uenishi, K., and Turner, W. M., "Three-Dimensional Upwinding Navier-Stokes Code with k-ε Model for Supersonic Flows," AIAA Paper 91-1669, June 1991.

[14]Carlson, J. R., "A Nozzle Internal Performance Prediction Method," NASA TP 3221, Oct. 1991.

[15]Jones, W. P., and Launder, B. E., "The Calculation of Low-Reynolds-Number Phenomena with a Two-Equation Model of Turbulence," *International Journal of Heat and Mass Transfer*, Vol. 16, 1973, pp. 1119–1130.